

A Footprint-Aware, High-Resolution Approach for Carbon Flux Prediction Across Diverse Ecosystems

Jacob Searcy^{1*}, Anish Dulal², Scott Bridgman^{3,4,5}, Ashley Cordes^{1,4}, Lillian Aoki^{3,4}, Brendan Bohannon^{3,5}, Qing Zhu⁶, Lucas C. R. Silva^{3,4,5}

¹ Department of Data Science, University of Oregon

² Department of Computer Science, University of Oregon

³ Institute of Ecology and Evolution, University of Oregon

⁴ Environmental Studies Program, University of Oregon

⁵ Department of Biology, University of Oregon

⁶ Climate and Ecosystem Sciences Division, Lawrence Berkeley National Lab

*Corresponding author: Jacob Searcy Email: jsearcy@uoregon.edu

Key Words: Carbon; Fluxes; Landsat; Upscaling; Remote Sensing; Machine Learning

Abstract: Natural climate solutions (NCS) offer an approach to mitigating carbon dioxide (CO₂) emissions. However, monitoring the carbon drawdown of ecosystems over large geographic areas remains challenging. Eddy-flux covariance towers provide ground truth for predictive ‘upscaling’ models derived from satellite products, but many satellites now produce measurements on spatial scales smaller than a flux tower’s footprint. We introduce Footprint-Aware Regression (FAR), a first-of-its-kind, deep-learning framework that simultaneously predicts spatial footprints and pixel-level (30 m scale) estimates of carbon flux. FAR is trained on our AMERI-FAR25 dataset which combines 439 site years of tower data with corresponding Landsat scenes. Our model produces high-resolution predictions and achieves $R^2 = 0.78$ when predicting monthly net ecosystem exchange on test sites from a variety of ecosystems.

1. Introduction

Climate change is an urgent global concern, posing significant risks to environmental stability, economic development, and human health ¹. While the decarbonization of energy systems through the reduction of fossil fuel emissions is critical, natural climate solutions (NCS) offer a complementary approach to mitigating climate change ^{2,3}. NCS includes a variety of strategies from conservation, restoration, and improved management of ecosystems to enhance carbon sequestration and reduce greenhouse gas emissions. In the US, NCS strategies are utilized to generate credits on voluntary carbon markets such as the American Carbon Registry (ACR) ⁴. However, the ACR methodologies for validating CO₂ drawdown require significant effort, and can involve numerous manual measurements across several sites, which accumulates error and is a barrier to both quick scaling of NCS strategies and to participation of smaller landowners ⁵. In this work, we propose a deep learning model that provides accurate CO₂ flux estimates at the high spatial resolutions appropriate for informing management practices using readily available remote sensing data.

The gold standard for land-based measurements of CO₂ flux are eddy covariance (EC) towers. EC towers measure CO₂ flux by tracking rapid fluctuations in vertical wind speed and gas concentrations as atmospheric eddies transport air parcels between the surface and the atmosphere. A major obstacle in utilizing EC tower data for predictive models is their measurement footprint, which is defined as the land area that contributes to the observed flux. This upwind footprint varies with tower height, ecosystem properties, and atmospheric conditions, and can span areas from 10³-10⁷ m² ⁶. These footprint sizes are significantly larger than the 900 m² pixels available from Landsat or high-resolution products such as the 13.7 m² products from Planet Labs ⁷. Landscapes also vary at much smaller spatial scales which can lead to tower measurements that integrate a variety of carbon sources and sinks within their footprint. There is growing evidence that accounting for this spatial heterogeneity is crucial for accurate gas flux estimation. For example, spatial representativeness within a heterogeneous landscape was the dominant uncertainty in upscaling net ecosystem production (NEP), or carbon sequestration in a 17 EC tower case study ⁸. Furthermore, the percentage of vegetation types within a tower's footprint varies from site to site, which potentially leads to footprint bias ^{6,9}. Difficulties with spatial heterogeneity have also been found in EC tower measurements of methane ¹⁰. There is evidence that such spatial heterogeneity could be accounted for by using high-resolution satellite data. For example, high-resolution satellite measurements within an EC tower's footprint have improved correlations with EC tower data ¹¹. However, there is currently no analysis method that can be used to account for spatial heterogeneity across EC tower networks. Machine learning could provide such a method, but existing machine learning datasets used for flux predictions lack high-resolution satellite imagery ¹².

In this paper, we present AMERI-FAR25, a first of its kind dataset of 439 site years of EC tower data and over 45,000 associated 30mx30m Landsat scenes (satellite images), combined with a novel deep learning framework (FAR) for high-resolution footprint-aware flux prediction across multiple EC networks. FAR (Footprint Aware Regression) incorporates features of process-based ecosystem models (for example, by including our current understanding of how CO₂ flux relates to environmental drivers), while simultaneously learning ecosystem properties from satellite data. It utilizes a novel attention mechanism (a technique that directs deep learning models to prioritize the most important aspects of input data) that directly models the measurement footprint of EC towers. We demonstrate that this approach can produce

predictions at the high spatial resolution and accuracy required to inform natural climate solutions at landowner scales.

2. Methods

2.1 FAR Overview

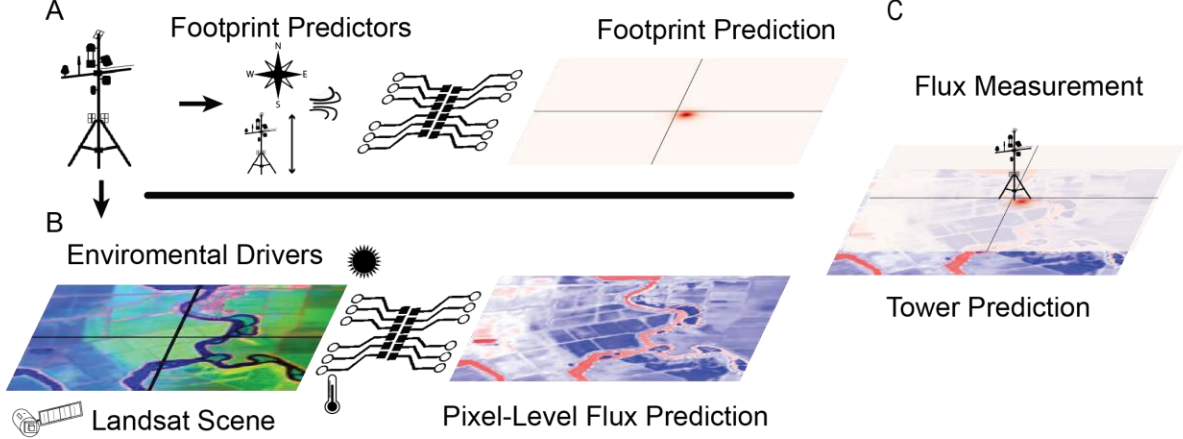


Figure 1 Model overview schematic. (A) Atmospheric variables from tower measurements are used to predict an attention mask to model an EC tower’s footprint. (B) Landsat-scene data and environmental drivers are used to create a pixel-level flux prediction. (C) Pixel-level predictions are weighted by the predicted footprint and the resulting prediction is trained on measured flux.

FAR utilizes the time-varying nature of EC tower footprints to understand fluxes at smaller spatial scales. Generally, high-resolution satellite imagery is only available at temporal scales that greatly exceed the half-hour measurements publicly available for most EC towers. However, FAR exploits the fact that the landscape measured by each satellite pixel will differentially contribute to the EC tower’s measurement depending on the atmospheric conditions that determine the tower’s footprint. Previous work in this area was explored by Xu et al.¹³, who developed an environmental response function technique that relates flux measurements to variables that were dynamically weighted and then averaged by the measurement footprint. FAR expands this work by producing pixel-level predictions directly, adding a learnable footprint model, and expanding training from one EC tower to a large network of EC towers.

FAR is depicted in Figure 1 and is divided into two parts that are aggregated to predict EC tower measurements. First, the pixel-level flux prediction model utilizes a grid of pixels from multi-band satellites centered at each flux tower with length L , width W , and D bands ($x_{landsat,T} \in \mathbb{R}^{L \times W \times D}$) and N local meteorological data points measured by the tower ($x_{drivers,t} \in \mathbb{R}^N$). This model predicts $FC_{pixel} \in \mathbb{R}^{L \times W}$, a gridded pixel-level prediction of CO₂ flux. Above, t denotes the sampling of tower measured variables (nominally every half-hour) and T denotes the sampling of the Landsat data using all available bands (nominally every 16 days per satellite). Second, the footprint prediction model utilizes M measurements related to the atmosphere tower ($x_{footprint,t} \in \mathbb{R}^M$) to predict a measurement footprint $FP \in \mathbb{R}^{L \times W}$ such that $\sum_{l,w} FP_{l,w} = 1$,

which acts as a weighted average of the input pixels . Both model arms are then combined to yield a single flux prediction for each time point \hat{y}_t . Where

$$\hat{y}_t = \sum_{l,w}^{L,W} FC_{l,w} (x_{landsat,T}, x_{drivers,t}; \theta) \odot FP_{l,w} (x_{footprint,t}; \theta) \quad 1$$

with \odot representing element-wise multiplication. Both arms were trained simultaneously to minimize the mean squared error of tower measurements ($y \in \mathbb{R}^1$) and the flux prediction FC_{tower} , using the loss function.

$$L = \sum_t MSE (y_t, \hat{y}_t) + \lambda \sum_{l,w} FP_{l,w} * \ln(FP_{l,w,t}) \quad 2$$

Where $\lambda \sum_{l,w} FP_{l,w} * \ln(FP_{l,w})$ is an entropy regularization term, with $\lambda > 0$ minimizing entropy to prefer small footprints, $\lambda < 0$ maximizing entropy to prefer large footprints, and $\lambda = 0$ applying no preference. This setup allows us to factorize flux prediction from any spatial biases arising from changing tower footprints. The flux prediction stage can then be used independently to obtain pixel level flux predictions.

The flux-prediction model was implemented with a simple multi-layer perceptron (MLP). This MLP is applied independently to each input pixel, with each environmental driver held constant across the input image. The footprint prediction model is also implemented with a simple MLP. $x_{footprint,t}$ are repeated to match the spatial extent of the image and coordinates $x_w, y_l \in 0 < \mathbb{R} < 1$ are concatenated as two new channels to allow for a single MLP to be applied pixel-wise to predict the footprint. The final output is constrained to sum to 1 by applying a softmax over the two spatial dimensions.

$$FP_{lw} = \text{softmax} \left(f(x_{footprint,t}, x_w, y_l) \right) \quad 3$$

We note that in order to learn a meaningful footprint there must be sufficient spatial heterogeneity in the dataset; however, a lack of spatial heterogeneity would imply that any footprint model would be sufficient since all pixels would have similar values, making this a simple add-on layer to any spatially explicit predictive task. We show empirically that AMERI-FAR25 has sufficient spatial heterogeneity that a learned footprint model improves predictions, and reproduces some features expected from theoretical calculations.

2.2 AMERI-FAR25 Dataset

The AMERI-FAR25 Dataset is 439 site years of EC tower data combined with 45,124 satellite scenes. We obtained EC tower data from the AmeriFlux BASE product ¹⁴ for all sites releasing data after 2013 under the CC-BY-4.0 license with downloadable half-hour flux data. Sites with missing measurements or metadata were dropped, and the remaining data were cleaned and harmonized resulting in 209 sites (see Appendix A). FAR’s footprint model utilized wind direction (WD), wind speed (WS), friction velocity (USTAR), air temperature (TA), sensible heat turbulent flux (H), and tower height (HEIGHT). FAR’s flux prediction model utilized the environmental drivers shortwave incoming radiation (SW_IN), air temperature (TA), and relative humidity (RH), and FAR’s prediction target was carbon flux (FC). In addition to tower

measurements, we obtained the 800 m daily normals for TA and RH (treated as constant throughout the day), and monthly normals solar transmission from for PRISM.¹⁵ Solar transmission was used in combination with the software package *pysolar*¹⁶ to estimate half-hour solar radiation at each site. Satellite data was taken from Landsat 8 and 9 Level 1 data. This data product contains 11 bands including 9 bands at 30 m resolution and 2 Thermal Infra bands at 100 m resolution resampled to 30 m. Together these bands provide significant information on vegetation and soil moisture for use in FAR. Patches of 128 x 128 pixels centered on each tower’s location were extracted from Landsat scenes. Scenes were processed to account for clouds and missing data. This reflects a working process where the most recently available information is used for prediction. For each Landsat patch, all bands except for the panchromatic one (which provides broad spectrum measurements at higher spatial resolution) are concatenated with four orientation angles (Solar/Sensor, Azimuth/Zenith) to form our input $x_{landsat,T}$. The resulting dataset we refer to as AMERI-FAR25 is a publicly available dataset that provides a large-scale pairing of satellite imagery and EC tower measurements.

2.3 Training and Evaluation

AMERI-FAR25 was split into training, validation, and test sets. Training sets were used during training to fit model weights. The validation sets were used during training to determine if a model was overfit, and the test sets were only used for evaluation. For testing FAR’s upscaling, the 209 sites were grouped by International Geosphere–Biosphere Programme (IGBP) definition codes (denoting ecosystem types, e.g. deciduous forest, wetland, etc.), and for all IGBP groups with 10 or more sites, 40% of those sites were withheld and evenly split between the validation (*val_site*) and test set (*test_site*). AMERI-FAR25 also provides splits to test forecasting or temporal drift *test_future* and *val_future*, which consist of the last year of data from every site with multiple years of data. In addition, 20% of points were withheld at random from the remaining data to make a final validation set (*val*).

Before training, targets and fluxes were scaled based on training data statistics to facilitate neural network training. To avoid bias in the footprint model toward prevailing wind directions, data augmentation was applied to each Landsat scene by rotating it and the wind direction by an arbitrary angle. FAR was trained until no further improvement was observed in the loss function in any of the validation sets. The *val* dataset achieved the lowest loss value, followed by *val_future* and *val_site*, which both achieved their minimum loss earlier in the training process. The weights with lowest loss on the *val_site* dataset were then used for subsequent evaluation, since it represents the best test of the upscaling task. Training was performed on the University of Oregon’s high-performance computer, Talapas, and took about 7 days on an A100 in MIG mode configured with 40GB of GPU memory.

To evaluate FAR, we assessed its performance in our *test_site* dataset across a variety of sites and IGBP codes using root mean squared error (RMSE), and coefficients of determination (R^2). FAR produces half-hour predictions, but to allow for easier comparisons with existing literature we integrated predictions into monthly sums except where noted. As a baseline we also compared FAR’s performance against XGBoost¹⁷, which has been widely used for upscaling¹⁸. For these baselines, we took the average of Landsat bands in a 5x5 pixel (150m x 150m) uniform footprint and used the resulting values and environmental drivers as inputs to these models. We also investigated feature importance to assess the model’s reliance on causal features, or lack thereof, using Shapely Additive Explanations (SHAP)¹⁹. SHAP values attribute each feature’s

contribution, positive or negative, to a given FC prediction. We compare learned footprints to a parametrized 2D model²⁰ FAR's footprint comparisons utilized additional variables, the Monin-Obukhov length and the standard deviation of lateral wind velocity fluctuations. For sites where these variables were not available they were predicted from the same variables used in FAR's footprint prediction arm. These values were then inputted into the footprint package²⁰ with an assumed boundary layer height of 1 km. The area for each footprint was calculated by combining the pixels with the largest attention values iteratively until their sum exceeded 0.95. Finally, to assess our ability to upscale, we replaced EC tower measurements with estimates derived from PRISM and applied our model to a large geographic area of Oregon as a demonstration of FARs utility.

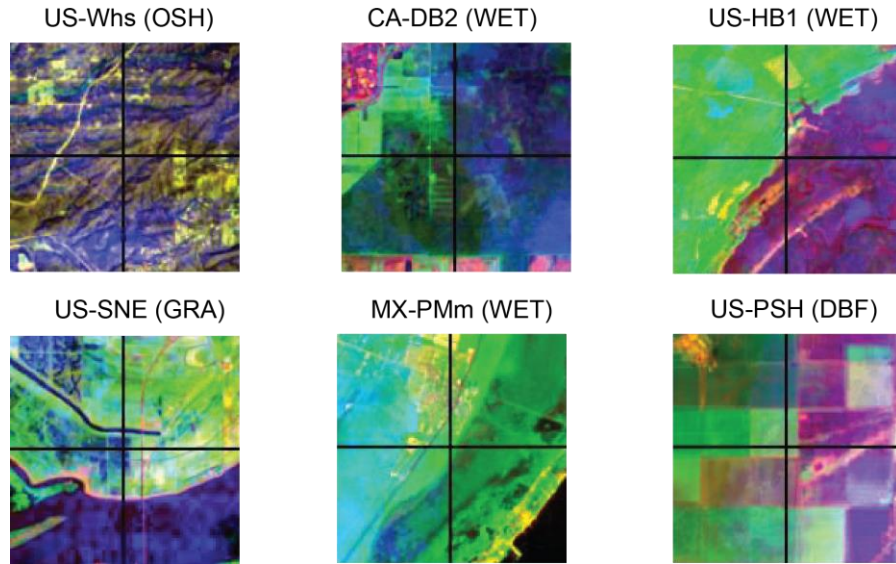


Figure 2 False color Landsat patches of sites with strong performance gains with FAR with respect to XGBoost. Crosshairs denote site center within the patch, text in parentheses represent the IGBP code of each site. In this representation, the spectral bands Red, NIR, and SWIR1 are equated with the images Red, Green, and Blue channels respectively.

3. Results

Table 1 FAR and XGBoost results at varying time scales. FAR outperforms XGBoost at all scales.

<i>Frequency</i>	<i>FAR R^2</i>	<i>XGBoost R^2</i>	<i>FAR RMSE (MGC/HA/YR)</i>	<i>XGBoost RMSE (MGC/HA/YR)</i>
<i>half-hour</i>	0.65	0.59	11.51	12.41
<i>monthly</i>	0.78	0.66	3.14	3.14
<i>yearly</i>	0.81	0.69	1.39	1.39

3.1 Flux Predictions

FAR predicted monthly FC in our withheld sites with high confidence across all sites ($R^2=0.78$, $RMSE = 0.21 \text{ Mg C ha}^{-1} \text{ mo}^{-1}$) in comparison to XGBoost ($R^2=0.66$, $RMSE = 0.26 \text{ Mg C ha}^{-1} \text{ mo}^{-1}$). Results at different temporal resolutions can be found in Table 1. Overall agreement between

EC measurements and predictions improves with longer time scales and consistently outperforms XGBoost.

As expected, sites showing the largest increase in R^2 when using FAR compared with XGBoost exhibit significant spatial heterogeneity. As an example, the six sites with the largest improvement in R^2 are shown in Figure 2. Each patch displays the average values of the available Landsat scenes in false color with R=Red, G=NIR, B=SWIR2. Several of these sites exist near boundaries or exhibit spatial heterogeneity nearby the tower. These sites have a mean tower height of 5.8 m, with the shortest, CA-DB2, being 2.5 m and the tallest MX-PMm being 8.5 m. Sites are located in the middle of each patch where the black guidelines intersect.

Figure 3 plots the SHAP value for each input feature and prediction, categorized based on our interpretation of each feature's role in the model. The six most significant features (those with the largest mean absolute SHAP value) in descending order are SW_IN, Red, Blue, SWIR 2, Near Infrared, and SWIR 1. This intuitive result corresponds with solar radiation being a key driver of carbon flux, followed by frequently used proxies for vegetation and soil moisture. For example, the normalized difference vegetation index (NDVI) is calculated from the Red and Near Infrared channels^{21,22} and its extension the enhanced vegetation index (EVI) incorporates the blue channel²³. Similarly, SWIR 1 and 2 are used in the normalized difference water index (NDWI)²⁴, and normalized burn ratio (NBR)²⁵ respectively. Together this implies that FAR uses well-known features to predict fluxes.

3.2 Footprints

The properties of the learned footprints depend on the value λ used during training to regularize the footprints. Across all λ 's, footprints learn the tower's location at the center of the image and the need to be up-wind, but their respective areas can vary significantly and yield comparable R^2 on the test data. For all results we utilize $\lambda = 1e^{-3}$ which yields the best $R^2 = 0.78$, with $\lambda = -1e^{-3}$ yielding an $R^2 = 0.76$, and $\lambda = 0$ yielding an $R^2 = 0.76$. Replacing the learned footprints with those estimated from the footprint package described by Kljun et al.²⁰ yields an $R^2 = 0.77$. Figure 4 shows that footprints generally must be up-wind and notably for all λ the learned footprints are larger than those predicted by Kljun et al. for towers less than 3 meters tall. This result is consistent with tracer studies²⁶.

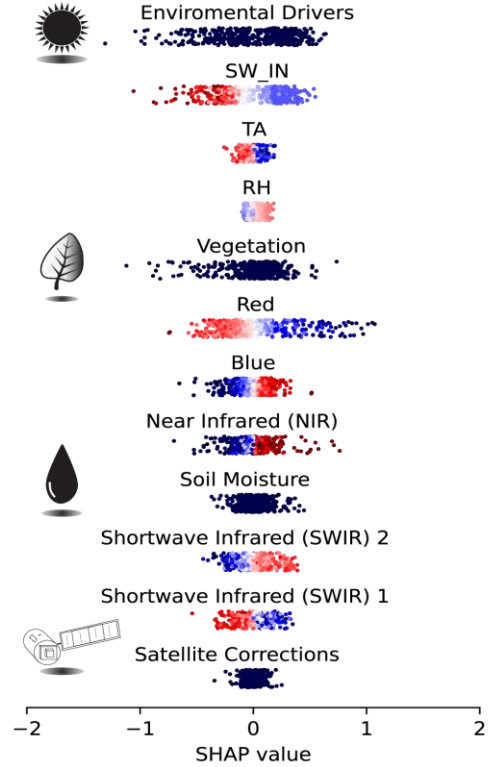


Figure 3 SHAP values for important model features. SHAP values are grouped into 4 categories 1. Environmental drivers (SW_IN, TA, RH), 2. Vegetation Proxies (Red, NIR, Blue, Green), 3. Soil Moisture (SWIR 1/2, TIRS 1/2, Coastal aerosol) and 4. Satellite Corrections (SAA, SZA, VAA, VZA, TIME_MASK, Cirrus). Below each group is a selection of the highest-impact features. These are shown with red/blue points denoting higher/lower than average values. Red points on the left of the figure denote a high value of that feature is associated with flux to the atmosphere, and blue points denote ecosystem drawdown.

Otherwise we interpret the fact that footprint areas can vary widely depending on λ , and still yield comparable results to imply insufficient radial heterogeneity at larger scales to refine the learned footprint model.

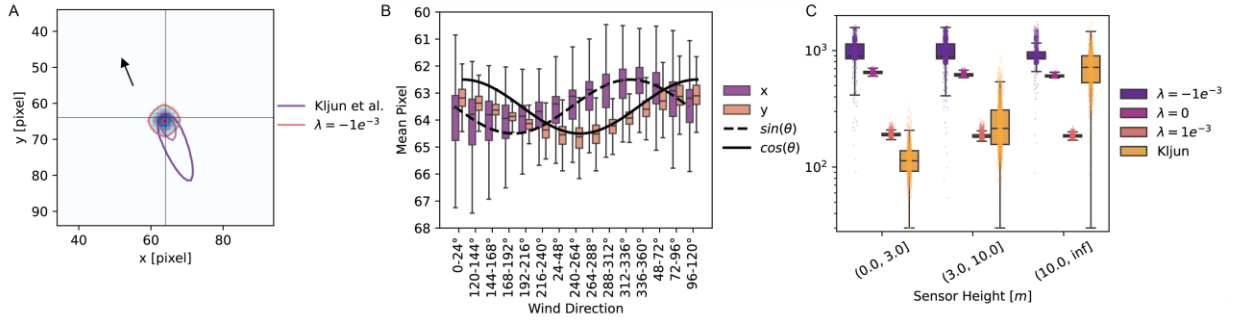


Figure 4 Learned Footprint Characteristics. (A) An example predicted footprint compared against Kljun et al. (arrow denotes wind direction) (B) The footprint weighted mean of the coordinates versus wind direction. (C) The square root of the area containing 95% of the footprint obtained from different models including Kljun et al. and FAR trained with different values of λ .

FAR generally learns a footprint that is more circular than Kljun et al., which may reflect variation of the footprint during the half-hour measurement, or averaging over unobserved site characteristics. Figure 5 shows how FAR’s footprint changes with key input variables. For all plots, a single random reference measurement was selected, and the values of the variable of interest were artificially changed and used to predict a new footprint. Fig. 5 A shows increasing footprint area at low friction velocity as expected, however, unexpectedly this curve reaches a minimum area at 0.6 ms^{-1} before continuing to increase at higher friction velocities. Data are significantly limited at higher friction velocities, which likely contributes to this behavior. Fig. 5 B shows area increasing with windspeed and Fig. 5 C shows increases with tower height. Changes in the area of the predicted footprint ($\sim 5.2\text{e}5 - 6.1\text{e}5 \text{ m}^2$) are small compared to Kljun et al., which as an example would predict $2.9\text{e}4 \text{ m}^2$ for a 6 m tower and $1.2\text{e}6 \text{ m}^2$ for 30 m tower for the same conditions used above.

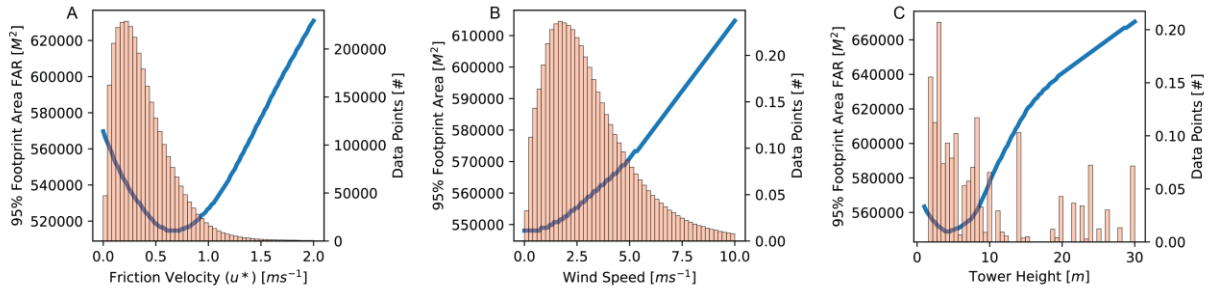


Figure 5 FAR Footprint Area versus Predictors. Each panel shows a blue line created from predictions of the $\lambda = 0$ model by scanning the variable on the x-axis while all other variables were held constant. The histogram on each plot shows the number of data points with a corresponding value. (A) Friction velocity, (B) Wind Speed, (C) Tower Height.

3.3 Results by Site and Upscaling

Figure 6b breaks down the RMSE for each test site grouped by their respective IGBP codes with R^2 scores for all predictions in that IGBP code. The IGBP codes with the highest R^2 were DBF (deciduous broadleaf forests, $R^2=0.86$), ENF (evergreen needle forests, $R^2=0.78$), and WET (wetlands, $R^2=0.76$). OSH (open shrublands) had the worst R^2 score, and one of the lowest RMSE. While this is slightly counterintuitive, this can be understood due to the relatively low flux observed at the OSH sites. The model is confident that the OSH fluxes are small, but explaining the remaining variance in these small fluxes remains a challenge. We also note that negative R^2 scores occur when FAR's predictions have a larger error than a prediction of the mean for that subset of data.

Three sites have high enough RMSEs to qualify as outliers (1.5x the interquartile range). The monthly predictions versus true measurements for these sites are shown in Figure 7. US-NC3 (Fig 7 A) is classified as ENF and was clear-cut in 2012 and replanted in 2013. The years 2013 and 2014 have the largest discrepancy with respect to the EC tower's measurement with FAR predicting net CO_2 drawdown for all months, and EC tower measuring net emissions. We hypothesize that the replanting may obscure signs of clear cutting leading to an underestimate of remaining emission sources. US-Oho is located in a Metro-Park with one year of data in AMERI-FAR25. FAR underestimates the site measurements, although it maintains a high overall correlation. Overall FAR performance is highest in forests but remains a useful predictor across several biomes.

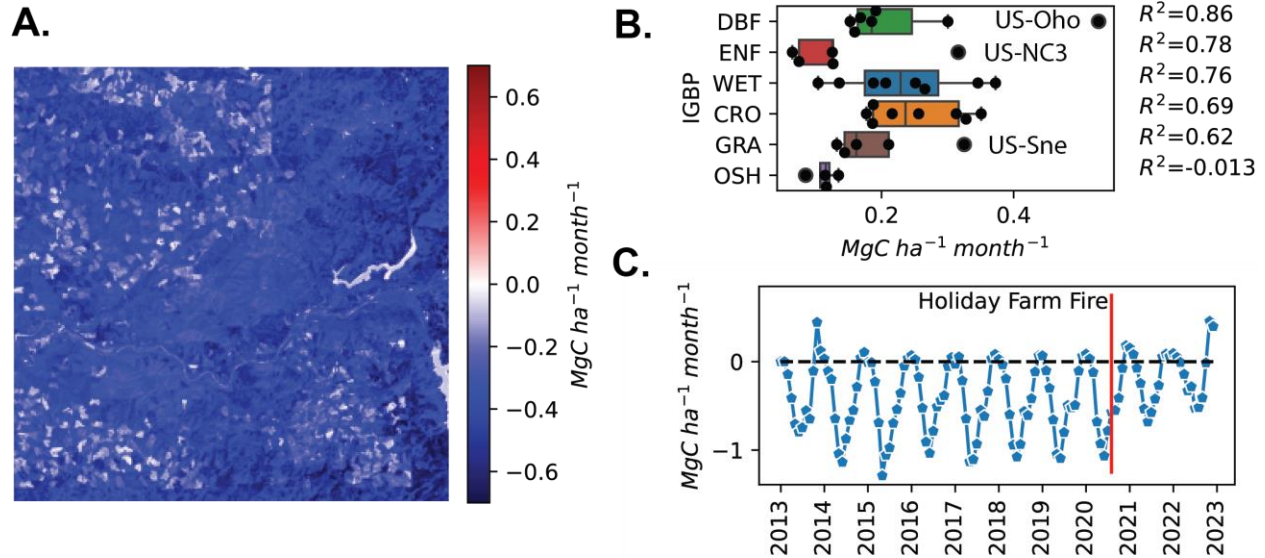


Figure 6 Results of the FAR model on test set, and its use in upscaling. (A) FAR applied to regional-sized area in Oregon centered on the HJ Andrews experimental forest. Emission sources are shown in red, and areas of high CO_2 drawdown are shown in blue. (B) The RMSE of every test site grouped by IGBP code, and the R^2 value for data with that IGBP code. (C) A decadal time series of predicted flux averaged across the area shown in (A). A large disturbance caused by the Holiday Farm Fire in September 2020 is denoted by a vertical line.

Replacing meteorological variables measured by each tower with values estimated from PRISM during inference results in nearly identical predictive power on test sites ($R^2=0.77$). Figure 6a demonstrates FAR applied to a regional-scale area with 30 m resolution centered on the HJ

Andrews Experimental Forest. The map shows fluxes temporally averaged over a 10-year period, with Figure 6c showing the time series of the same region spatially averaged. Of note is the large Holiday Farm Fire that swept the area in Fall 2020 and significantly shifted predictions toward higher emissions afterward.

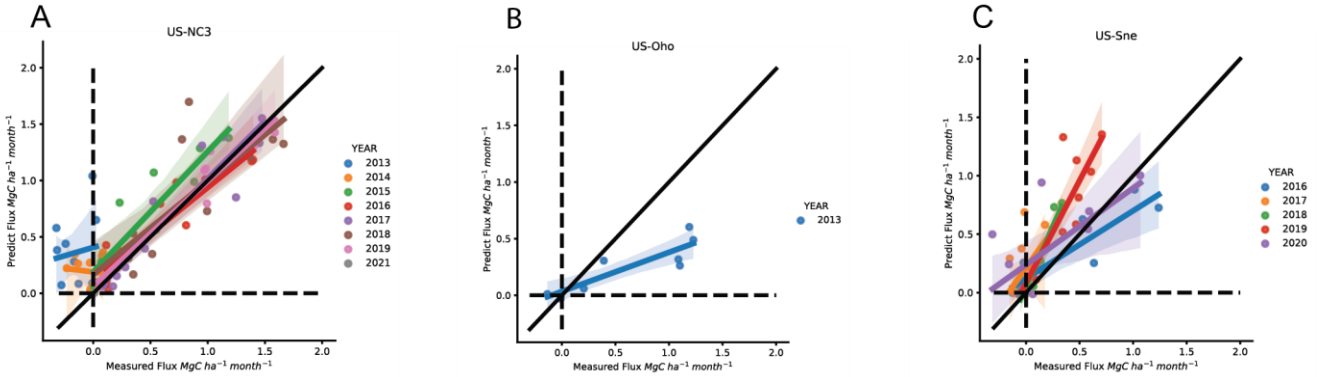


Figure 7 Monthly Predictions vs. Measurements for Outlier Sites. (A) US-NC3 (ENF) (B) US-Oho (DBF) and (C) US-SNE (GRA). Each plot contains best fit lines for each year of data; positive values represent CO₂ drawdown from the atmosphere to the environment.

4. Discussion

We have shown that FAR effectively uses a novel attention mechanism to address a key challenge of varying spatial scales when upscaling EC carbon flux estimates. We also have provided the AMERI-FAR25 dataset to enable future studies using this, or a similar, technique. FAR had superior performance compared to frequently used XGBoost methods, and FAR can provide pixel-level predictions at spatial resolutions smaller than that of an EC tower's footprint, which improves predictions in sites with spatial heterogeneity.

FAR is well suited for broader application on current and future efforts to harmonize EC tower data globally. However, there are several limitations of FAR. The data to train FAR are concentrated in North America, and similarly the use of PRISM for upscaling currently is limited to the USA. Another important assumption of FAR is that the input environmental drivers are sufficient to predict an ecosystem's response, which is unlikely to be true for urban or intensively managed areas with a variety of additional CO₂ sources and where additional data may be needed to predict ecosystem fluxes.

Despite accurate and precise results in a variety of ecosystems, there remains progress to be made in predicting some outlier sites shortly after interventions such as replanting. Additional environmental drivers, site features, or historical information may be required to capture the observed differences in those sites. FAR's framework could also be used to predict CH₄ fluxes with appropriate environmental drivers. Despite its limitations, FAR provides high accuracy upscaling for many wetlands and forest types, at higher resolutions than has previously been possible, paving the way for easier validation of natural climate solutions, and working toward easier access to these markets for smaller landowners.

Our findings demonstrate that FAR can resolve the long-standing challenge of footprint bias in spatiotemporal predictions and translate EC data into maps of carbon fluxes. By integrating 439

site-years of flux tower measurements with Landsat imagery, FAR not only achieves high predictive ability across diverse ecosystems but also provides a generalizable framework for estimating ecosystem sinks and sources of CO₂ at scales directly relevant to land management and policy. Importantly, this opens the door to calculating carbon budgets across heterogeneous landscapes, offering an avenue to reconcile ecosystem processes with local and regional assessments of climate mitigation potential. The ability to quantify both expected and outlier dynamics (e.g. disturbance legacies, land-use transitions, or climate extremes) will advance understanding of the coupled feedback among ecosystems, land use, and the atmosphere. FAR thus represents a significant step toward building the empirical foundations needed for solutions to be evaluated not only in terms of potential, but also in terms of realized carbon drawdown and resilience to future change, and to test ecological theory integrating bottom-up flux measurements into top-down carbon monitoring.

References

1. Intergovernmental Panel on Climate Change (IPCC). Key Risks across Sectors and Regions. *Climate Change 2022 – Impacts, Adaptation and Vulnerability* 2411–2538 (2023) doi:10.1017/9781009325844.025.
2. *Climate Change 2022 - Mitigation of Climate Change*. (Cambridge University Press, 2023). doi:10.1017/9781009157926.
3. Silva, L. C. R. *et al.* A generalizable framework for enhanced natural climate solutions. *Plant and Soil* 2022 479:1 479, 3–24 (2022).
4. World's First Private Carbon Crediting Program for Offsets - ACR. <https://acrcarbon.org/>.
5. Taylor, A. How to integrate remote sensing into the forest carbon market, the right way - ACR. <https://acrcarbon.org/news/how-to-integrate-remote-sensing-into-the-forest-carbon-market-the-right-way/>.
6. Chu, H. *et al.* Representativeness of Eddy-Covariance flux footprints for areas surrounding AmeriFlux sites. *Agric For Meteorol* 301–302, 108350 (2021).
7. Planet Labs: Satellite Imagery & Earth Data Analytics. <https://www.planet.com/>.
8. Ran, Y. *et al.* Spatial representativeness and uncertainty of eddy covariance carbon flux measurements for upscaling net ecosystem productivity to the grid scale. *Agric For Meteorol* 230–231, 114–127 (2016).
9. Fang, J. *et al.* Assessing Spatial Representativeness of Global Flux Tower Eddy-Covariance Measurements Using Data from FLUXNET2015. *Scientific Data* 2024 11:1 11, 1–16 (2024).
10. Peltola, O. *et al.* Studying the spatial variability of methane flux with five eddy covariance towers of varying height. *Agric For Meteorol* 214–215, 456–472 (2015).
11. Kong, J. *et al.* Matching high resolution satellite data and flux tower footprints improves their agreement in photosynthesis estimates. *Agric For Meteorol* 316, 108878 (2022).
12. Fortier, M., Richter, M. L., Sonnentag, O. & Pal, C. CarbonSense: A Multimodal Dataset and Baseline for Carbon Flux Modelling.
13. Xu, K., Metzger, S. & Desai, A. R. Upscaling tower-observed turbulent exchange at fine spatio-temporal resolution using environmental response functions. *Agric For Meteorol* 232, 10–22 (2017).
14. Chu, H. *et al.* AmeriFlux BASE data pipeline to support network growth and data sharing. *Scientific Data* 2023 10:1 10, 1–13 (2023).
15. PRISM Group at Oregon State University. <https://prism.oregonstate.edu/terms/>.
16. Pysolar: staring directly at the sun since 2007 — Pysolar 0.8rc2 documentation. <https://pysolar.readthedocs.io/en/latest/>.

17. Chen, T. & Guestrin, C. XGBoost: A Scalable Tree Boosting System. *Proceedings of the 22nd ACM SIGKDD International Conference on Knowledge Discovery and Data Mining* <https://doi.org/10.1145/2939672> doi:10.1145/2939672.
18. Zhu, S., Quaife, T. & Hill, T. Uniform upscaling techniques for eddy covariance FLUXes (UFLUX). *Int J Remote Sens* **45**, 1450–1476 (2024).
19. Lundberg, S. M., Allen, P. G. & Lee, S.-I. A Unified Approach to Interpreting Model Predictions. *Adv Neural Inf Process Syst* **30**, (2017).
20. Kljun, N., Calanca, P., Rotach, M. W. & Schmid, H. P. A simple two-dimensional parameterisation for Flux Footprint Prediction (FFP). *Geosci Model Dev* **8**, 3695–3713 (2015).
21. Tucker, C. J. Red and photographic infrared linear combinations for monitoring vegetation. *Remote Sens Environ* **8**, 127–150 (1979).
22. Rouse, J. W. , Jr., Haas, R. H., Schell, J. A. & Deering, D. W. Monitoring vegetation systems in the Great Plains with ERTS. *NASA. Goddard Space Flight Center 3d ERTS-1 Symp., Vol. 1, Sect. A* (1974).
23. Huete, A. *et al.* Overview of the radiometric and biophysical performance of the MODIS vegetation indices. *Remote Sens Environ* **83**, 195–213 (2002).
24. Gao, B. C. NDWI—A normalized difference water index for remote sensing of vegetation liquid water from space. *Remote Sens Environ* **58**, 257–266 (1996).
25. Key, C. & Benson, N. The Normalized Burn Ratio (NBR): A Landsat TM radiometric index of burn severity. in *USGS/NPS Joint Fire Science Conference Proceedings* (U.S. Geological Survey, National Park Service, Remote Sensing Applications Center., Boise, Idaho, 1999).
26. Rey-Sanchez, C. *et al.* Detecting Hot Spots of Methane Flux Using Footprint-Weighted Flux Maps. *J Geophys Res Biogeosci* **127**, e2022JG006977 (2022).
27. Tamburrini, G. The AI Carbon Footprint and Responsibilities of AI Scientists. *Philosophies* 2022, Vol. 7, Page 4 **7**, 4 (2022).
28. Henderson, P. *et al.* Towards the Systematic Reporting of the Energy and Carbon Footprints of Machine Learning. *Journal of Machine Learning Research* **21**, 1–43 (2020).
29. Where your power comes from | EWEB. <https://www.eweb.org/your-public-utility/power-supply>.
30. Technology-specific Cost and Performance Parameters — IPCC. <https://www.ipcc.ch/report/ar5/wg3/technology-specific-cost-and-performance-parameters/>.
31. Dauble, D. D., Hanrahan, T. P., Geist, D. R. & Parsley, M. J. Impacts of the Columbia River hydroelectric system on main-stem habitats of fall chinook salmon. *N Am J Fish Manag* **23**, 641–659 (2003).
32. Lee, K. N. The Columbia river basin. Experimenting with sustainability. *Environment* vol. 31 Preprint at <https://doi.org/10.1080/00139157.1989.9928950> (1989).
33. yannforget/landsatxplore: Search and download Landsat scenes from EarthExplorer. <https://github.com/yannforget/landsatxplore>.
34. jsearcy1/landsatxplore: Search and download Landsat scenes from EarthExplorer. <https://github.com/jsearcy1/landsatxplore>.
35. Ronneberger, O., Fischer, P. & Brox, T. U-Net: Convolutional Networks for Biomedical Image Segmentation. *Lecture Notes in Computer Science (including subseries Lecture Notes in Artificial Intelligence and Lecture Notes in Bioinformatics)* **9351**, 234–241 (2015).

36. Paszke, A. *et al.* PyTorch: An Imperative Style, High-Performance Deep Learning Library. <https://doi.org/10.5555/3454287.3455008> (2019) doi:10.5555/3454287.3455008.
37. Kingma, D. P. & Ba, J. L. Adam: A Method for Stochastic Optimization. *3rd International Conference on Learning Representations, ICLR 2015 - Conference Track Proceedings* <https://arxiv.org/abs/1412.6980v9> (2014).
38. Posse, G. AmeriFlux AmeriFlux AR-CCg Carlos Casares grassland. Preprint at (2022).
39. Kutzbach, L. AmeriFlux AmeriFlux AR-TF1 Rio Moat bog. Preprint at (2019).
40. Kutzbach, L. AmeriFlux AmeriFlux AR-TF2 Rio Pipo bog. Preprint at (2019).
41. Antonino, A. AmeriFlux AmeriFlux BR-CST Caatinga Serra Talhada. Preprint at (2019).
42. Vourlitis, G., Dalmagro, H., de S. Nogueira José and Johnson, M. & Arruda, P. AmeriFlux AmeriFlux BR-Npw Northern Pantanal Wetland. Preprint at (2019).
43. Todd, A. & Humphreys, E. AmeriFlux AmeriFlux CA-ARB Attawapiskat River Bog. Preprint at (2018).
44. Todd, A. & Humphreys, E. AmeriFlux AmeriFlux CA-ARF Attawapiskat River Fen. Preprint at (2018).
45. Garneau, M. AmeriFlux AmeriFlux CA-BOU Bouleau Peatland. Preprint at (2023).
46. Knox, S. AmeriFlux AmeriFlux CA-DB2 Delta Burns Bog 2. Preprint at (2021).
47. Christen, A. & Knox, S. AmeriFlux AmeriFlux CA-DBB Delta Burns Bog. Preprint at (2019).
48. Knox, S. AmeriFlux AmeriFlux CA-DSM Delta Salt Marsh. Preprint at (2023).
49. Wagner-Riddle, C. AmeriFlux AmeriFlux CA-ER1 Elora Research Station. Preprint at (2019).
50. McCaughey, H. AmeriFlux AmeriFlux CA-Gro Ontario - Groundhog River, Boreal Mixedwood Forest. Preprint at (2016).
51. Black, T. AmeriFlux AmeriFlux CA-LP1 British Columbia - Mountain pine beetle-attacked lodgepole pine stand. Preprint at (2020).
52. Arain, M. AmeriFlux AmeriFlux CA-TP1 Ontario - Turkey Point 2002 Plantation White Pine. Preprint at (2016).
53. Arain, M. AmeriFlux AmeriFlux CA-TP3 Ontario - Turkey Point 1974 Plantation White Pine. Preprint at (2016).
54. Arain, M. AmeriFlux AmeriFlux CA-TP4 Ontario - Turkey Point 1939 Plantation White Pine. Preprint at (2016).
55. Arain, M. AmeriFlux AmeriFlux CA-TPD Ontario - Turkey Point Mature Deciduous. Preprint at (2016).
56. Perez-Quezada, J. & Armesto, J. AmeriFlux AmeriFlux CL-SDF Senda Darwin Forest. Preprint at (2022).
57. Alvarado-Barrientos, M. AmeriFlux AmeriFlux MX-PMm Puerto Morelos mangrove. Preprint at (2021).
58. Roman, T. *et al.* AmeriFlux AmeriFlux PE-QFR Quistococha Forest Reserve. Preprint at (2020).
59. NEON (National Ecological Observatory Network). AmeriFlux AmeriFlux PR-xGU NEON Guanica Forest (GUAN). Preprint at (2021).
60. NEON (National Ecological Observatory Network). AmeriFlux AmeriFlux PR-xLA NEON Lajas Experimental Station (LAJA). Preprint at (2021).
61. Billesbach, D., Kueppers, L., Torn, M. & Biraud, S. AmeriFlux AmeriFlux US-A32 ARM-SGP Medford hay pasture. Preprint at (2018).
62. Billesbach, D., Kueppers, L., Torn, M. & Biraud, S. AmeriFlux AmeriFlux US-A74 ARM SGP milo field. Preprint at (2018).

63. Olson, B. AmeriFlux AmeriFlux US-ALQ Allequash Creek Site. Preprint at (2018).
64. Biraud, S., Fischer, M., Chan, S. & Torn, M. AmeriFlux AmeriFlux US-ARM ARM Southern Great Plains site- Lamont. Preprint at (2016).
65. Anderson, R. AmeriFlux AmeriFlux US-ASH USSL San Joaquin Valley Almond High Salinity. Preprint at (2020).
66. Anderson, R. AmeriFlux AmeriFlux US-ASL USSL San Joaquin Valley Almond Low Salinity. Preprint at (2020).
67. Anderson, R. AmeriFlux AmeriFlux US-ASM USSL San Joaquin Valley Almond Medium Salinity. Preprint at (2020).
68. Rocha, A., Shaver, G. & Hobbie, J. AmeriFlux AmeriFlux US-An1 Anaktuvuk River Severe Burn. Preprint at (2016).
69. Rocha, A., Shaver, G. & Hobbie, J. AmeriFlux AmeriFlux US-An2 Anaktuvuk River Moderate Burn. Preprint at (2016).
70. Rocha, A., Shaver, G. & Hobbie, J. AmeriFlux AmeriFlux US-An3 Anaktuvuk River Unburned. Preprint at (2016).
71. Novick, K. AmeriFlux AmeriFlux US-BRG Bayles Road Grassland Tower. Preprint at (2021).
72. Euskirchen, E. AmeriFlux AmeriFlux US-BZB Bonanza Creek Thermokarst Bog. Preprint at (2021).
73. Euskirchen, E. AmeriFlux AmeriFlux US-BZF Bonanza Creek Rich Fen. Preprint at (2021).
74. Euskirchen, E. AmeriFlux AmeriFlux US-BZS Bonanza Creek Black Spruce. Preprint at (2021).
75. Euskirchen, E. AmeriFlux AmeriFlux US-BZo Bonanza Creek Old Thermokarst Bog. Preprint at (2022).
76. Richardson, A. & Hollinger, D. AmeriFlux AmeriFlux US-Bar Bartlett Experimental Forest. Preprint at (2016).
77. Rey-Sanchez, C. *et al.* AmeriFlux AmeriFlux US-Bi1 Bouldin Island Alfalfa. Preprint at (2018).
78. Rey-Sanchez, C. *et al.* AmeriFlux AmeriFlux US-Bi2 Bouldin Island corn. Preprint at (2018).
79. Phillips, C. & Huggins, D. AmeriFlux AmeriFlux US-CF1 CAF-LTAR Cook East. Preprint at (2019).
80. Huggins, D. AmeriFlux AmeriFlux US-CF2 CAF-LTAR Cook West. Preprint at (2019).
81. Huggins, D. AmeriFlux AmeriFlux US-CF3 CAF-LTAR Boyd North. Preprint at (2019).
82. Huggins, D. AmeriFlux AmeriFlux US-CF4 CAF-LTAR Boyd South. Preprint at (2019).
83. Oikawa, P. AmeriFlux AmeriFlux US-CGG Concord Grazed Grassland. Preprint at (2023).
84. Davis, K. AmeriFlux AmeriFlux US-CLF Cole Farm. Preprint at (2023).
85. Scott, R. AmeriFlux AmeriFlux US-CMW Charleston Mesquite Woodland. Preprint at (2020).
86. Ewers, B., Bretfeld, M. & Pendall, E. AmeriFlux AmeriFlux US-CPk Chimney Park. Preprint at (2016).
87. Noormets, A. AmeriFlux AmeriFlux US-CRK Davy Crockett National Forest. Preprint at (2023).
88. Chen, J. & Chu, H. AmeriFlux AmeriFlux US-CRT Curtice Walter-Berger cropland. Preprint at (2016).

89. Desai, A. AmeriFlux AmeriFlux US-CS1 Central Sands Irrigated Agricultural Field. Preprint at (2020).
90. Desai, A. AmeriFlux AmeriFlux US-CS2 Tri county school Pine Forest. Preprint at (2020).
91. Desai, A. AmeriFlux AmeriFlux US-CS3 Central Sands Irrigated Agricultural Field. Preprint at (2020).
92. Desai, A. AmeriFlux AmeriFlux US-CS4 Central Sands Irrigated Agricultural Field. Preprint at (2021).
93. Desai, A. AmeriFlux AmeriFlux US-CS5 Central Sands Irrigated Agricultural Field. Preprint at (2022).
94. Desai, A. AmeriFlux AmeriFlux US-CS6 Central Sands Irrigated Agricultural Field. Preprint at (2023).
95. Desai, A. AmeriFlux AmeriFlux US-CS8 Central Sands Irrigated Agricultural Field. Preprint at (2023).
96. Clark, K. AmeriFlux AmeriFlux US-Ced Cedar Bridge. Preprint at (2016).
97. Duff, A. & Desai, A. AmeriFlux AmeriFlux US-DFC US Dairy Forage Research Center, Prairie du Sac. Preprint at (2020).
98. Duff, A., Desai, A. & Risso, V. AmeriFlux AmeriFlux US-DFK Dairy Forage Research Center - Kernza. Preprint at (2021).
99. Hinkle, C. & Bracho, R. AmeriFlux AmeriFlux US-DPW Disney Wilderness Preserve Wetland. Preprint at (2019).
100. Schuppenhauer, M., Biraud, S. & Deverel Steve and Chan, S. AmeriFlux AmeriFlux US-DS3 Staten Rice 1. Preprint at (2022).
101. Arias-Ortiz, A. & Baldocchi, D. AmeriFlux AmeriFlux US-Dmg Dutch Slough Marsh Gilbert Tract. Preprint at (2023).
102. Oikawa, P. AmeriFlux AmeriFlux US-EDN Eden Landing Ecological Reserve. Preprint at (2019).
103. Starr, G. & Oberbauer, S. AmeriFlux AmeriFlux US-Elm Everglades (long hydroperiod marsh). Preprint at (2016).
104. Starr, G. & Oberbauer, S. AmeriFlux AmeriFlux US-Esm Everglades (short hydroperiod marsh). Preprint at (2016).
105. Ueyama, M., Iwata, H. & Harazono, Y. AmeriFlux AmeriFlux US-Fcr Cascaden Ridge Fire Scar. Preprint at (2019).
106. Spence, C. AmeriFlux AmeriFlux US-GL1 Stannard Rock. Preprint at (2023).
107. Frank, J. & Massman, B. AmeriFlux AmeriFlux US-GLE GLEES. Preprint at (2016).
108. Forsythe, J., Kline, M. & O'Halloran, T. AmeriFlux AmeriFlux US-HB1 North Inlet Crab Haul Creek. Preprint at (2020).
109. Forsythe, J., Kline, M. & O'Halloran, T. AmeriFlux AmeriFlux US-HB2 Hobcaw Barony Mature Longleaf Pine. Preprint at (2020).
110. Forsythe, J., Kline, M. & O'Halloran, T. AmeriFlux AmeriFlux US-HB3 Hobcaw Barony Longleaf Pine Restoration. Preprint at (2020).
111. Kelsey, E. & Green, M. AmeriFlux AmeriFlux US-HBK Hubbard Brook Experimental Forest. Preprint at (2020).
112. Runkle, B. AmeriFlux AmeriFlux US-HRA Humnoke Farm Rice Field - AWD. Preprint at (2019).
113. Reba, M. AmeriFlux AmeriFlux US-HRC Humnoke Farm Rice Field - conventional. Preprint at (2019).

114. Liu, H., Huang, M. & Chen, X. AmeriFlux AmeriFlux US-Hn2 Hanford 100H grassland. Preprint at (2019).
115. Liu, H., Huang, M. & Chen, X. AmeriFlux AmeriFlux US-Hn3 Hanford 100H sagebrush. Preprint at (2019).
116. Hollinger, D. AmeriFlux AmeriFlux US-Ho1 Howland Forest (main tower). Preprint at (2016).
117. Hollinger, D. AmeriFlux AmeriFlux US-Ho2 Howland Forest (west tower). Preprint at (2016).
118. Arias-Ortiz, A., Szutu, D., Verfaillie, J. & Baldocchi, D. AmeriFlux AmeriFlux US-Hsm Hill Slough Marsh. Preprint at (2022).
119. Matamala, R. AmeriFlux AmeriFlux US-IB1 Fermi National Accelerator Laboratory-Batavia (Agricultural site). Preprint at (2016).
120. Matamala, R. AmeriFlux AmeriFlux US-IB2 Fermi National Accelerator Laboratory-Batavia (Prairie site). Preprint at (2016).
121. Euskirchen, E., Shaver, G. & Bret-Harte, S. AmeriFlux AmeriFlux US-ICh Imnavait Creek Watershed Heath Tundra. Preprint at (2016).
122. Euskirchen, E., Shaver, G. & Bret-Harte, S. AmeriFlux AmeriFlux US-ICs Imnavait Creek Watershed Wet Sedge Tundra. Preprint at (2016).
123. Euskirchen, E., Shaver, G. & Bret-Harte, S. AmeriFlux AmeriFlux US-ICt Imnavait Creek Watershed Tussock Tundra. Preprint at (2016).
124. Vivoni, E. & Perez-Ruiz, E. AmeriFlux AmeriFlux US-Jo2 Jornada Experimental Range Mixed Shrubland. Preprint at (2020).
125. Brunsell, N. AmeriFlux AmeriFlux US-KFS Kansas Field Station. Preprint at (2016).
126. Brunsell, N. AmeriFlux AmeriFlux US-KLS Kansas Land Institute. Preprint at (2019).
127. Sullivan, P. AmeriFlux AmeriFlux US-KPL Lily Lake Fen. Preprint at (2022).
128. Bracho, R. & Hinkle, C. AmeriFlux AmeriFlux US-KS3 Kennedy Space Center (salt marsh). Preprint at (2019).
129. Brunsell, N. AmeriFlux AmeriFlux US-Kon Konza Prairie LTER (KNZ). Preprint at (2016).
130. Wood, J. & Gu, L. AmeriFlux AmeriFlux US-MOz Missouri Ozark Site. Preprint at (2016).
131. Law, B. AmeriFlux AmeriFlux US-Me2 Metolius-intermediate aged ponderosa pine. Preprint at (2016).
132. Law, B. AmeriFlux AmeriFlux US-Me6 Metolius Young Pine Burn. Preprint at (2016).
133. Desai, A. AmeriFlux AmeriFlux US-Men Lake Mendota, Center for Limnology Site. Preprint at (2018).
134. Schreiner-McGraw, A. AmeriFlux AmeriFlux US-Mo1 LTAR CMRB Field 1 (CMRB ASP). Preprint at (2022).
135. Schreiner-McGraw, A. AmeriFlux AmeriFlux US-Mo2 LTAR CMRB Tucker Prairie (CMRB TP). Preprint at (2022).
136. Schreiner-McGraw, A. AmeriFlux AmeriFlux US-Mo3 LTAR CMRB Field 3 (CMRB BAU). Preprint at (2022).
137. Litvak, M. AmeriFlux AmeriFlux US-Mpj Mountainair Pinyon-Juniper Woodland. Preprint at (2016).
138. Matthes, J. *et al.* AmeriFlux AmeriFlux US-Myb Mayberry Wetland. Preprint at (2016).
139. Noormets, A. *et al.* AmeriFlux AmeriFlux US-NC2 NC_Loblolly Plantation. Preprint at (2016).
140. Noormets, A. *et al.* AmeriFlux AmeriFlux US-NC3 NC_Clearcut#3. Preprint at (2018).

141. Noormets, A. *et al.* AmeriFlux AmeriFlux US-NC4 NC_AlligatorRiver. Preprint at (2018).
142. Torn, M. & Dengel, S. AmeriFlux AmeriFlux US-NGB NGEE Barrow. Preprint at (2018).
143. Torn, M. & Dengel, S. AmeriFlux AmeriFlux US-NGC NGEE Arctic Council. Preprint at (2020).
144. Niwot Ridge US-NR1 30-min data. Preprint at (2016).
145. Knowles, J. AmeriFlux AmeriFlux US-NR3 Niwot Ridge Alpine (T-Van West). Preprint at (2021).
146. Knowles, J. AmeriFlux AmeriFlux US-NR4 Niwot Ridge Alpine (T-Van East). Preprint at (2021).
147. Silveira, M. & Bracho, R. AmeriFlux AmeriFlux US-ONA Florida pine flatwoods. Preprint at (2020).
148. Bohrer, G. AmeriFlux AmeriFlux US-ORv Olentangy River Wetland Research Park. Preprint at (2016).
149. Bohrer, G. & Kerns, J. AmeriFlux AmeriFlux US-OWC Old Woman Creek. Preprint at (2018).
150. Chen, J., Chu, H. & Noormets, A. AmeriFlux AmeriFlux US-Oho Oak Openings. Preprint at (2016).
151. Anderson, R. AmeriFlux AmeriFlux US-PSH USSL San Joaquin Valley Pistachio High. Preprint at (2020).
152. Anderson, R. AmeriFlux AmeriFlux US-PSL USSL San Joaquin Valley Pistachio Low. Preprint at (2020).
153. Desai, A. AmeriFlux AmeriFlux US-Pnp Lake Mendota, Picnic Point Site. Preprint at (2018).
154. Iwahana, G., Kobayashi, H., Ikawa, H. & Suzuki, R. AmeriFlux AmeriFlux US-Prr Poker Flat Research Range Black Spruce Forest. Preprint at (2016).
155. Schuppenhauer, M., Biraud, S. & Chan, S. AmeriFlux AmeriFlux US-RGA Arkansas Corn Farm. Preprint at (2022).
156. Schuppenhauer, M., Biraud, S. & Chan, S. AmeriFlux AmeriFlux US-RGB Butte County Rice Farm. Preprint at (2022).
157. Schuppenhauer, M., Biraud, S. & Chan, S. AmeriFlux AmeriFlux US-RGF Stanislaus County Forage Farm. Preprint at (2023).
158. Schuppenhauer, M., Biraud, S. & Chan, S. AmeriFlux AmeriFlux US-RGW Desha County Rice Farm. Preprint at (2022).
159. Schuppenhauer, M., Biraud, S. & Chan, S. AmeriFlux AmeriFlux US-RGo Glenn County Organic Rice Farm. Preprint at (2022).
160. Flerchinger, G. AmeriFlux AmeriFlux US-Rls RCEW Low Sagebrush. Preprint at (2018).
161. Flerchinger, G. AmeriFlux AmeriFlux US-Rms RCEW Mountain Big Sagebrush. Preprint at (2017).
162. Baker, J., Griffis, T. & Griffis, T. AmeriFlux AmeriFlux US-Ro1 Rosemount- G21. Preprint at (2016).
163. Baker, J. & Griffis, T. AmeriFlux AmeriFlux US-Ro2 Rosemount- C7. Preprint at (2018).
164. Baker, J. & Griffis, T. AmeriFlux AmeriFlux US-Ro4 Rosemount Prairie. Preprint at (2018).
165. Baker, J. & Griffis, T. AmeriFlux AmeriFlux US-Ro5 Rosemount I18_South. Preprint at (2018).
166. Baker, J. & Griffis, T. AmeriFlux AmeriFlux US-Ro6 Rosemount I18_North. Preprint at (2018).

167. Ueyama, M., Iwata, H. & Harazono, Y. AmeriFlux AmeriFlux US-Rpf Poker Flat Research Range: Succession from fire scar to deciduous forest. Preprint at (2019).
168. Flerchinger, G. AmeriFlux AmeriFlux US-Rwf RCEW Upper Sheep Prescribed Fire. Preprint at (2020).
169. Flerchinger, G. AmeriFlux AmeriFlux US-Rws Reynolds Creek Wyoming big sagebrush. Preprint at (2017).
170. Bracho, R. & Martin, T. AmeriFlux AmeriFlux US-SP1 Slashpine-Austin Cary- 65yrs nat regen. Preprint at (2016).
171. Kurc, S. AmeriFlux AmeriFlux US-SRC Santa Rita Creosote. Preprint at (2016).
172. Scott, R. AmeriFlux AmeriFlux US-SRG Santa Rita Grassland. Preprint at (2016).
173. Scott, R. AmeriFlux AmeriFlux US-SRM Santa Rita Mesquite. Preprint at (2016).
174. Vivoni, E. AmeriFlux AmeriFlux US-SRS Santa Rita Experimental Range Mesquite Savanna. Preprint at (2020).
175. Forsythe, B., Horne, J. & Davis, K. AmeriFlux AmeriFlux US-SSH Susquehanna Shale Hills Critical Zone Observatory. Preprint at (2022).
176. Litvak, M. AmeriFlux AmeriFlux US-Seg Sevilleta grassland. Preprint at (2016).
177. Litvak, M. AmeriFlux AmeriFlux US-Ses Sevilleta shrubland. Preprint at (2016).
178. Clark, K. AmeriFlux AmeriFlux US-Slt Silas Little- New Jersey. Preprint at (2016).
179. Detto, M., Sturtevant, C., Oikawa, P., Verfaillie, J. & Baldocchi, D. AmeriFlux AmeriFlux US-Snd Sherman Island. Preprint at (2016).
180. Shortt, R., Hemes, K., Szutu, D., Verfaillie, J. & Baldocchi, D. AmeriFlux AmeriFlux US-Sne Sherman Island Restored Wetland. Preprint at (2018).
181. Kusak, K., Sanchez, C., Szutu, D. & Baldocchi, D. AmeriFlux AmeriFlux US-Snf Sherman Barn. Preprint at (2019).
182. Bergamaschi, B. & Windham-Myers, L. AmeriFlux AmeriFlux US-Srr Suisun marsh - Rush Ranch. Preprint at (2018).
183. Vargas, R. AmeriFlux AmeriFlux US-StJ St Jones Reserve. Preprint at (2018).
184. Desai, A. AmeriFlux AmeriFlux US-Syv Sylvania Wilderness Area. Preprint at (2016).
185. Valach, A. *et al.* AmeriFlux AmeriFlux US-Tw1 Twitchell Wetland West Pond. Preprint at (2016).
186. Sturtevant, C., Verfaillie, J. & Baldocchi, D. AmeriFlux AmeriFlux US-Tw2 Twitchell Corn. Preprint at (2016).
187. Chamberlain, S. *et al.* AmeriFlux AmeriFlux US-Tw3 Twitchell Alfalfa. Preprint at (2016).
188. Eichelmann, E. *et al.* AmeriFlux AmeriFlux US-Tw4 Twitchell East End Wetland. Preprint at (2016).
189. Valach, A., Kasak, K., Szutu, D., Verfaillie, J. & Baldocchi, D. AmeriFlux AmeriFlux US-Tw5 East Pond Wetland. Preprint at (2019).
190. Knox, S., Matthes, J., Verfaillie, J. & Baldocchi, D. AmeriFlux AmeriFlux US-Twt Twitchell Island. Preprint at (2016).
191. Bohrer, G. AmeriFlux AmeriFlux US-UM3 Douglas Lake. Preprint at (2018).
192. Gough, C., Bohrer, G. & Curtis, P. AmeriFlux AmeriFlux US-UMB Univ. Of Mich. Biological station. Preprint at (2016).
193. Ladig, K. & Inkenbrandt, P. AmeriFlux AmeriFlux US-UTB UFLUX Bonneville Salt Flats. Preprint at (2023).
194. Ueyama, M., Iwata, H. & Harazono, Y. AmeriFlux AmeriFlux US-Uaf University of Alaska, Fairbanks. Preprint at (2018).

195. Ma, S., Xu, L., Verfaillie, J. & Baldocchi, D. AmeriFlux AmeriFlux US-Var Vaira Ranch-Ione. Preprint at (2016).
196. Litvak, M. AmeriFlux AmeriFlux US-Vcm Valles Caldera Mixed Conifer. Preprint at (2016).
197. Litvak, M. AmeriFlux AmeriFlux US-Vcp Valles Caldera Ponderosa Pine. Preprint at (2016).
198. Litvak, M. AmeriFlux AmeriFlux US-Vcs Valles Caldera Sulphur Springs Mixed Conifer. Preprint at (2018).
199. Chen, J. & Chu, H. AmeriFlux AmeriFlux US-WPT Winous Point North Marsh. Preprint at (2016).
200. Scott, R. AmeriFlux AmeriFlux US-Whs Walnut Gulch Lucky Hills Shrub. Preprint at (2016).
201. Litvak, M. AmeriFlux AmeriFlux US-Wjs Willard Juniper Savannah. Preprint at (2016).
202. Scott, R. AmeriFlux AmeriFlux US-Wkg Walnut Gulch Kendall Grasslands. Preprint at (2016).
203. Wharton, S. AmeriFlux AmeriFlux US-Wrc Wind River Crane Site. Preprint at (2016).
204. NEON (National Ecological Observatory Network). AmeriFlux AmeriFlux US-xAB NEON Abby Road (ABBY). Preprint at (2020).
205. NEON (National Ecological Observatory Network). AmeriFlux AmeriFlux US-xAE NEON Klemme Range Research Station (OAES). Preprint at (2020).
206. NEON (National Ecological Observatory Network). AmeriFlux AmeriFlux US-xBA NEON Barrow Environmental Observatory (BARR). Preprint at (2020).
207. NEON (National Ecological Observatory Network). AmeriFlux AmeriFlux US-xBL NEON Blandy Experimental Farm (BLAN). Preprint at (2020).
208. NEON (National Ecological Observatory Network). AmeriFlux AmeriFlux US-xBN NEON Caribou Creek - Poker Flats Watershed (BONA). Preprint at (2020).
209. NEON (National Ecological Observatory Network). AmeriFlux AmeriFlux US-xBR NEON Bartlett Experimental Forest (BART). Preprint at (2019).
210. NEON (National Ecological Observatory Network). AmeriFlux AmeriFlux US-xCL NEON LBJ National Grassland (CLBJ). Preprint at (2020).
211. NEON (National Ecological Observatory Network). AmeriFlux AmeriFlux US-xCP NEON Central Plains Experimental Range (CPER). Preprint at (2019).
212. NEON (National Ecological Observatory Network). AmeriFlux AmeriFlux US-xDC NEON Dakota Coteau Field School (DCFS). Preprint at (2020).
213. NEON (National Ecological Observatory Network). AmeriFlux AmeriFlux US-xDJ NEON Delta Junction (DEJU). Preprint at (2020).
214. NEON (National Ecological Observatory Network). AmeriFlux AmeriFlux US-xDL NEON Dead Lake (DELA). Preprint at (2019).
215. NEON (National Ecological Observatory Network). AmeriFlux AmeriFlux US-xDS NEON Disney Wilderness Preserve (DSNY). Preprint at (2020).
216. NEON (National Ecological Observatory Network). AmeriFlux AmeriFlux US-xGR NEON Great Smoky Mountains National Park, Twin Creeks (GRSM). Preprint at (2020).
217. NEON (National Ecological Observatory Network). AmeriFlux AmeriFlux US-xHA NEON Harvard Forest (HARV). Preprint at (2019).
218. NEON (National Ecological Observatory Network). AmeriFlux AmeriFlux US-xHE NEON Healy (HEAL). Preprint at (2020).
219. NEON (National Ecological Observatory Network). AmeriFlux AmeriFlux US-xJE NEON Jones Ecological Research Center (JERC). Preprint at (2020).

220. NEON (National Ecological Observatory Network). AmeriFlux AmeriFlux US-xJR
NEON Jornada LTER (JORN). Preprint at (2020).
221. NEON (National Ecological Observatory Network). AmeriFlux AmeriFlux US-xKA
NEON Konza Prairie Biological Station - Relocatable (KONA). Preprint at (2019).
222. NEON (National Ecological Observatory Network). AmeriFlux AmeriFlux US-xKZ
NEON Konza Prairie Biological Station (KONZ). Preprint at (2019).
223. NEON (National Ecological Observatory Network). AmeriFlux AmeriFlux US-xLE
NEON Lenoir Landing (LENO). Preprint at (2021).
224. NEON (National Ecological Observatory Network). AmeriFlux AmeriFlux US-xMB
NEON Moab (MOAB). Preprint at (2020).
225. NEON (National Ecological Observatory Network). AmeriFlux AmeriFlux US-xML
NEON Mountain Lake Biological Station (MLBS). Preprint at (2020).
226. NEON (National Ecological Observatory Network). AmeriFlux AmeriFlux US-xNG
NEON Northern Great Plains Research Laboratory (NOGP). Preprint at (2020).
227. NEON (National Ecological Observatory Network). AmeriFlux AmeriFlux US-xNQ
NEON Onaqui-Ault (ONAQ). Preprint at (2020).
228. NEON (National Ecological Observatory Network). AmeriFlux AmeriFlux US-xNW
NEON Niwot Ridge Mountain Research Station (NIWO). Preprint at (2020).
229. NEON (National Ecological Observatory Network). AmeriFlux AmeriFlux US-xRM
NEON Rocky Mountain National Park, CASTNET (RMNP). Preprint at (2019).
230. NEON (National Ecological Observatory Network). AmeriFlux AmeriFlux US-xRN
NEON Oak Ridge National Lab (ORNL). Preprint at (2021).
231. NEON (National Ecological Observatory Network). AmeriFlux AmeriFlux US-xSB
NEON Ordway-Swisher Biological Station (OSBS). Preprint at (2020).
232. NEON (National Ecological Observatory Network). AmeriFlux AmeriFlux US-xSC
NEON Smithsonian Conservation Biology Institute (SCBI). Preprint at (2020).
233. NEON (National Ecological Observatory Network). AmeriFlux AmeriFlux US-xSE
NEON Smithsonian Environmental Research Center (SERC). Preprint at (2020).
234. NEON (National Ecological Observatory Network). AmeriFlux AmeriFlux US-xSJ
NEON San Joaquin Experimental Range (SJER). Preprint at (2020).
235. NEON (National Ecological Observatory Network). AmeriFlux AmeriFlux US-xSL
NEON North Sterling, CO (STER). Preprint at (2020).
236. NEON (National Ecological Observatory Network). AmeriFlux AmeriFlux US-xSP
NEON Soaproot Saddle (SOAP). Preprint at (2020).
237. NEON (National Ecological Observatory Network). AmeriFlux AmeriFlux US-xSR
NEON Santa Rita Experimental Range (SRER). Preprint at (2019).
238. NEON (National Ecological Observatory Network). AmeriFlux AmeriFlux US-xST
NEON Steigerwaldt Land Services (STEI). Preprint at (2020).
239. NEON (National Ecological Observatory Network). AmeriFlux AmeriFlux US-xTA
NEON Talladega National Forest (TALL). Preprint at (2020).
240. NEON (National Ecological Observatory Network). AmeriFlux AmeriFlux US-xTL
NEON Toolik (TOOL). Preprint at (2020).
241. NEON (National Ecological Observatory Network). AmeriFlux AmeriFlux US-xTR
NEON Treehaven (TREE). Preprint at (2020).
242. NEON (National Ecological Observatory Network). AmeriFlux AmeriFlux US-xUK
NEON The University of Kansas Field Station (UKFS). Preprint at (2020).

- 243. NEON (National Ecological Observatory Network). AmeriFlux AmeriFlux US-xUN
NEON University of Notre Dame Environmental Research Center (UNDE). Preprint at
(2020).
- 244. NEON (National Ecological Observatory Network). AmeriFlux AmeriFlux US-xWD
NEON Woodworth (WOOD). Preprint at (2019).
- 245. NEON (National Ecological Observatory Network). AmeriFlux AmeriFlux US-xWR
NEON Wind River Experimental Forest (WREF). Preprint at (2020).
- 246. NEON (National Ecological Observatory Network). AmeriFlux AmeriFlux US-xYE
NEON Yellowstone Northern Range (Frog Rock) (YELL). Preprint at (2020).

Acknowledgments

Funding

This material is based upon work supported by the National Science Foundation under Grant No 2319597 (LS, JS, AC, LA, BB). We acknowledge the AmeriFlux data portal as critical to this work. Funding for the AmeriFlux data portal was provided by the U.S. Department of Energy Office of Science.

Author contributions

Conceptualization: JS LS

Data Curation: JS AD QZ

Software: JS AD

Methodology: JS AD

Visualization: JS AD

Funding acquisition: LS, JS, AC, LA, BB, SB

Project administration: LS

Supervision: JS

Writing – original draft: JS AC

Writing – review & editing: KS LS BB SB AC LA QZ AD

Competing interests:

The authors declare that they have no competing interests.

Data and materials availability

The datasets and models used in this study will be available from online repositories when published. FAR's source code and pretrained weights are available on github and Zenodo. AMERI-FAR25 is available on Zenodo.

Resource Use Acknowledgment

There are increasing calls for AI scientists to acknowledge energy use and the tensions created using AI with promises to improve climate mitigation^{27,28}. To support this ethical standard, we report and acknowledge FAR's resource usage here. FAR was trained at the University of Oregon on a high-performance computing cluster utilizing one A100 GPU and associated compute infrastructure. While resources are shared on UO's HPC, this node's peak power usage is 2.4 kW and training took approximately 7 days, resulting in a maximum power usage of 403 kWh. Talapas uses Eugene's relatively low carbon-footprint supply of power which is primarily sourced from hydropower, followed by nuclear and biomass²⁹. We utilize the median IPCC's technology-specific performance parameters³⁰ for this power mix and estimate equivalent emissions of 22.4 kg eCO₂, or the equivalent of using about 2.5 gallons of gasoline. While this is relatively small, the extensive use of hydropower has greatly impacted the wellbeing of Indigenous Peoples in the Columbia Gorge and across the state of Oregon. Salmon habitats have been dramatically changed by the presence of hydropower in the Columbia and Snake Rivers for the past 60 years^{31,32}. The fall Chinook salmon, a species that reached near extinction in Oregon in the early 2020s and who are sacred kin of Indigenous Peoples, has

struggled with spawning in the alluvial river ecosystems due to insufficient modifications of dams and artificial flows.

Declaration of generative AI and AI-assisted technologies in the manuscript preparation process

During the preparation of this work the authors used ChatGPT-5 to improve the clarity and grammar of the manuscript. After using this tool, the authors reviewed and edited the content as needed and take full responsibility for the content of the published article.

Appendix A - AMERI-FAR25 Dataset

We obtained EC tower data from the AmeriFlux BASE product¹⁴ for all sites releasing data under the CC-BY-4.0 license with downloadable half-hour flux data. We required sites to have measurements of wind direction (WD), wind speed (WS), carbon flux (FC), friction velocity (USTAR), air temperature (TA), sensible heat turbulent flux (H), and relative humidity (RH); any sites without these variables were excluded. The remaining sites were required to have a measure of incoming radiation, either shortwave (SW_IN) or photosynthetic flux density (PPFD_IN). SW_IN was used for sites where SW_IN was available. For sites with only PPFD_IN available, SW_IN was predicted with a linear scaling of PPFD_IN. Sites without existing tower height metadata were then dropped resulting in 209 sites. For stations with multiple sensors measuring the same quantity, the highest sensor(s) was utilized, and replicates at this height were averaged. Outlier FC measurements exceeding 0.5% and 99.5% percentiles were dropped to prevent divergences during training, as were non-physical measurements that contained negative SW_IN values, and biologically implausible measurements where carbon drawdown ($FC < 0$) was measured with no incoming radiation (e.g. nighttime where $SW_IN=0$). In addition to tower measurements, we obtained the 800 m daily normals for PRISM¹⁵ data for TA and RH (treated as constant throughout the day), and monthly normals solar transmission from PRISM was used in combination with the software package *pysolar*¹⁶ to estimate half-hour solar radiation at each site. This resulted in 209 sites with 7,697,145 half-hour measurements (see Table A1 for full site list).

Satellite data was taken from Landsat 8 and 9 Level 1 data. This data product contains 11 bands including 9 bands at 30 m resolution and 2 Thermal Infra bands at 100 m resolution resampled to 30 m. These bands are Coastal aerosol (0.43-0.45 μm), Blue (0.45-0.51 μm), Green (0.53-0.59 μm), Red (0.64-0.67 μm), Near Infrared (NIR) (0.85-0.88 μm), Shortwave Infrared (SWIR) 1 (1.57-1.65 μm), SWIR 2 (2.11-2.29 μm), Panchromatic (0.50-0.68 μm), Cirrus (1.36-1.28 μm), Thermal Infrared (TIRS) 1 (10.6-11.19 μm) and TIRS 2 (11.50-12.51 μm). Together these bands provide significant information on vegetation and soil moisture for use in FAR. Landsat scenes that contained a flux tower were downloaded with the *landsatxplore* tool^{33,34}, with some updates made by the authors³⁴. Patches of 128 x 128 pixels centered on each tower's location were extracted from Landsat scenes resulting in 45,124 Landsat patches. Scenes were processed so pixels that were missing, cloudy ($PIXEL_QA \neq \{21824, 21888, 21952\}$), or bad data were replaced with the most recently available value for that pixel. This reflects a working process where the most recently available information is used for prediction. For each Landsat patch, all bands except for the panchromatic one (which provides broad spectrum measurements at higher spatial resolution) are concatenated with four orientation angles (Solar/Sensor, Azimuth/Zenith) to form our input $x_{landsat,T}$. Environmental drivers $x_{drivers,t}$ are comprised of SW_IN, TA, and RH. Footprint prediction variables $x_{footprint,t}$ are the concatenation of WD, WS, USTAR, TA, and H. The resulting dataset we refer to as AMERI-FAR25 is the first publicly available dataset that provides a large-scale pairing of satellite imagery and EC tower measurements.

AMERI-FAR25 was split into training, validation and test sets. Training sets were used during training to fit model weights. The validation sets were used during training to determine if a model was overfit, and the test sets were only used for evaluation. For testing FAR's upscaling, the 209 sites were grouped by IGBP code (denoting ecosystem types, e.g. deciduous forest,

wetland, etc.), and for all IGBP groups with 10 or more sites; 40% of those sites were withheld and evenly split between the validation (*val_site*) and test set (*test_site*). AMERI-FAR25 also provides splits to test forecasting or temporal drift *test_future* and *val_future*, which consist of the last year of data from every site with multiple years of data; however, these sets were not utilized in this study. In addition, 20% of points were withheld at random from the remaining data to make a final validation set (*val*).

Machine Learning Implementations

FAR's flux prediction model was implemented with a simple multi-layer perceptron (MLP), with 3 layers each with 512 hidden dimensions. This architecture was chosen over other possibilities such as U-Net³⁵ to improve generalization by preserving the independence of each pixel's prediction. The footprint prediction model is also implemented with a simple multi-layer perceptron, with 3 layers each with 512 hidden dimensions. The model was implemented in PyTorch³⁶ and trained with the Adam optimizer³⁷ using a learning rate of 1e-4.

Table A1 Sites used in AMERI-FAR25: The complete list of AmeriFlux sites used in each dataset split in AMERI-FAR25. Sites are exclusively divided between *train*, *val_site* and *test_site*, with sites in the train dataset also appearing in the *val* and *val_future* and *test_future* datasets.

<i>Site ID</i>	<i>IGBP</i>	<i>Date Range</i>	<i>Train Site Days</i>	<i>Test Site Days (site/future)</i>	<i>Val Site Days (site/future/val)</i>
<i>AR-CCg</i> ³⁸	GRA	2018-2021	359.6	0/0	0/230/137
<i>AR-TF1</i> ³⁹	WET	2016-2018	162.6	0/0	0/162/71
<i>AR-TF2</i> ⁴⁰	WET	2016-2017	0.0	0/0	202/0/0
<i>BR-CST</i> ⁴¹	DNF	2014-2015	1.3	0/123	0/0/8
<i>BR-Npw</i> ⁴²	WSA	2014-2017	221.3	0/0	0/118/68
<i>CA-ARB</i> ⁴³	WET	2013-2015	320.8	0/0	0/303/66
<i>CA-ARF</i> ⁴⁴	WET	2013-2015	380.1	0/0	0/190/77
<i>CA-BOU</i> ⁴⁵	WET	2018-2020	93.7	0/0	0/37/11
<i>CA-DB2</i> ⁴⁶	WET	2020-2020	0.0	189/0	0/0/0
<i>CA-DBB</i> ⁴⁷	WET	2016-2020	0.0	0/0	1030/0/0
<i>CA-DSM</i> ⁴⁸	WET	2022-2022	120.5	0/0	0/0/28
<i>CA-ER1</i> ⁴⁹	CRO	2015-2021	0.0	937/0	0/0/0
<i>CA-Gro</i> ⁵⁰	MF	2013-2014	0.0	0/0	0/278/0
<i>CA-LP1</i> ⁵¹	ENF	2013-2022	1014.3	0/268	0/0/258
<i>CA-TP1</i> ⁵²	ENF	2013-2017	0.0	0/0	1322/0/0
<i>CA-TP3</i> ⁵³	ENF	2013-2017	981.2	0/324	0/0/233
<i>CA-TP4</i> ⁵⁴	ENF	2013-2017	0.0	0/0	960/0/0
<i>CA-TPD</i> ⁵⁵	DBF	2013-2017	588.3	0/0	0/150/87
<i>CL-SDF</i> ⁵⁶	EBF	2014-2022	376.3	0/0	0/67/72
<i>MX-PMm</i> ⁵⁷	WET	2017-2018	0.0	153/0	0/0/0
<i>PE-QFR</i> ⁵⁸	WET	2018-2019	72.1	0/0	0/127/11
<i>PR-xGU</i> ⁵⁹	EBF	2019-2022	94.3	0/64	0/0/17
<i>PR-xLA</i> ⁶⁰	GRA	2018-2022	102.5	0/66	0/0/17
<i>US-A32</i> ⁶¹	GRA	2015-2017	70.5	0/0	0/157/15
<i>US-A74</i> ⁶²	CRO	2016-2017	76.9	0/0	0/81/33
<i>US-ALQ</i> ⁶³	WET	2018-2023	640.1	0/157	0/0/116
<i>US-ARM</i> ⁶⁴	CRO	2013-2023	1346.6	0/225	0/0/375
<i>US-ASH</i> ⁶⁵	DBF	2016-2017	0.0	0/67	0/0/0
<i>US-ASL</i> ⁶⁶	DBF	2016-2017	0.0	0/0	0/22/0

<i>US-ASM</i> ⁶⁷	DBF	2016-2017	0.0	0/0	0/74/0
<i>US-An1</i> ⁶⁸	OSH	2013-2019	207.0	0/43	0/0/34
<i>US-An2</i> ⁶⁹	OSH	2013-2019	237.2	0/57	0/0/44
<i>US-An3</i> ⁷⁰	OSH	2013-2019	253.9	0/58	0/0/76
<i>US-BRG</i> ⁷¹	GRA	2017-2020	317.0	0/97	0/0/54
<i>US-BZB</i> ⁷²	WET	2014-2022	1350.9	0/0	0/260/341
<i>US-BZF</i> ⁷³	WET	2014-2022	1272.6	0/188	0/0/328
<i>US-BZS</i> ⁷⁴	ENF	2015-2021	851.5	0/0	0/217/222
<i>US-BZo</i> ⁷⁵	WET	2018-2022	0.0	820/0	0/0/0
<i>US-Bar</i> ⁷⁶	DBF	2013-2022	0.0	1164/0	0/0/0
<i>US-Bi1</i> ⁷⁷	CRO	2016-2023	0.0	1025/0	0/0/0
<i>US-Bi2</i> ⁷⁸	CRO	2017-2023	567.4	0/0	0/119/136
<i>US-CF1</i> ⁷⁹	CRO	2017-2022	566.4	0/0	0/164/114
<i>US-CF2</i> ⁸⁰	CRO	2017-2021	0.0	0/0	617/0/0
<i>US-CF3</i> ⁸¹	CRO	2017-2022	0.0	0/0	613/0/0
<i>US-CF4</i> ⁸²	CRO	2017-2021	439.1	0/137	0/0/91
<i>US-CGG</i> ⁸³	GRA	2019-2022	185.1	0/284	0/0/52
<i>US-CLF</i> ⁸⁴	CVM	2017-2020	44.9	0/0	0/101/4
<i>US-CMW</i> ⁸⁵	DBF	2013-2022	1772.8	0/283	0/0/340
<i>US-CPk</i> ⁸⁶	ENF	2013-2014	0.0	0/0	75/0/0
<i>US-CRK</i> ⁸⁷	ENF	2022-2022	48.3	0/0	0/0/9
<i>US-CRT</i> ⁸⁸	CRO	2013-2013	0.0	0/0	130/0/0
<i>US-CS1</i> ⁸⁹	CRO	2018-2019	0.0	0/0	0/173/0
<i>US-CS2</i> ⁹⁰	ENF	2018-2022	374.0	0/20	0/0/75
<i>US-CS3</i> ⁹¹	CRO	2019-2020	0.0	0/246	0/0/0
<i>US-CS4</i> ⁹²	CRO	2020-2021	0.0	0/0	0/210/0
<i>US-CS5</i> ⁹³	CRO	2021-2021	104.4	0/0	0/0/26
<i>US-CS6</i> ⁹⁴	CRO	2022-2023	0.0	175/0	0/0/0
<i>US-CS8</i> ⁹⁵	CRO	2023-2023	86.0	0/0	0/0/11
<i>US-Ced</i> ⁹⁶	CSH	2013-2015	126.8	0/188	0/0/19
<i>US-DFC</i> ⁹⁷	CRO	2018-2023	0.0	0/0	492/0/0
<i>US-DFK</i> ⁹⁸	CRO	2018-2021	0.0	278/0	0/0/0
<i>US-DPW</i> ⁹⁹	WET	2013-2016	365.8	0/312	0/0/100
<i>US-DS3</i> ¹⁰⁰	CRO	2021-2023	131.6	0/0	0/123/14
<i>US-Dmg</i> ¹⁰¹	WET	2021-2022	24.7	0/149	0/0/13
<i>US-EDN</i> ¹⁰²	WET	2018-2019	78.4	0/0	0/154/31
<i>US-Elm</i> ¹⁰³	WET	2013-2013	48.2	0/0	0/0/24
<i>US-Esm</i> ¹⁰⁴	WET	2013-2013	39.0	0/0	0/0/9
<i>US-Fcr</i> ¹⁰⁵	OSH	2013-2014	74.8	0/114	0/0/14
<i>US-GL1</i> ¹⁰⁶	WAT	2013-2021	911.5	0/0	0/246/215
<i>US-GLE</i> ¹⁰⁷	ENF	2013-2020	906.6	0/0	0/182/186
<i>US-HB1</i> ¹⁰⁸	WET	2019-2023	0.0	1112/0	0/0/0
<i>US-HB2</i> ¹⁰⁹	ENF	2019-2019	175.0	0/0	0/0/52
<i>US-HB3</i> ¹¹⁰	ENF	2019-2023	675.8	0/311	0/0/165
<i>US-HBK</i> ¹¹¹	DBF	2016-2022	0.0	594/0	0/0/0
<i>US-HRA</i> ¹¹²	CRO	2015-2017	0.0	61/0	0/0/0
<i>US-HRC</i> ¹¹³	CRO	2015-2017	29.7	0/0	0/30/5
<i>US-Hn2</i> ¹¹⁴	GRA	2018-2019	79.8	0/0	0/0/8
<i>US-Hn3</i> ¹¹⁵	OSH	2017-2019	5.6	0/0	0/102/0
<i>US-Ho1</i> ¹¹⁶	ENF	2017-2020	211.9	0/146	0/0/32
<i>US-Ho2</i> ¹¹⁷	ENF	2017-2020	0.0	329/0	0/0/0
<i>US-Hsm</i> ¹¹⁸	WET	2021-2023	214.5	0/160	0/0/37

<i>US-IB1</i> ¹¹⁹	CRO	2013-2018	911.5	0/169	0/0/162
<i>US-IB2</i> ¹²⁰	GRA	2013-2018	0.0	0/0	1375/0/0
<i>US-ICH</i> ¹²¹	OSH	2013-2021	0.0	2048/0	0/0/0
<i>US-ICs</i> (113)	WET	2014-2022	0.0	0/0	1886/0/0
<i>US-ICt</i> (114)	OSH	2013-2022	0.0	0/0	1748/0/0
<i>US-Jo2</i> (115)	OSH	2014-2021	896.6	0/0	0/145/181
<i>US-KFS</i> (116)	GRA	2013-2018	402.4	0/0	0/69/79
<i>US-KLS</i> (117)	GRA	2013-2019	0.0	0/0	526/0/0
<i>US-KPL</i> (118)	WET	2021-2022	0.0	380/0	0/0/0
<i>US-KS3</i> (119)	WET	2018-2019	0.0	0/179	0/0/0
<i>US-Kon</i> (120)	GRA	2013-2018	0.0	0/0	641/0/0
<i>US-MOz</i> (121)	DBF	2013-2022	1920.8	0/0	0/260/401
<i>US-Me2</i> (122)	ENF	2013-2022	0.0	0/0	2510/0/0
<i>US-Me6</i> (123)	ENF	2013-2022	1682.7	0/0	0/237/307
<i>US-Men</i> (124)	WAT	2013-2018	238.9	0/56	0/0/39
<i>US-Mo1</i> (125)	CRO	2015-2022	0.0	0/0	1836/0/0
<i>US-Mo2</i> (126)	GRA	2018-2023	0.0	1120/0	0/0/0
<i>US-Mo3</i> (127)	CRO	2016-2022	1192.9	0/0	0/293/188
<i>US-Mpj</i> (128)	ENF	2013-2023	2023.9	0/282	0/0/516
<i>US-Myb</i> (129)	WET	2013-2021	1733.9	0/261	0/0/387
<i>US-NC2</i> (130)	ENF	2013-2023	0.0	0/0	1139/0/0
<i>US-NC3</i> (131)	ENF	2013-2021	0.0	875/0	0/0/0
<i>US-NC4</i> (132)	WET	2015-2021	415.5	0/0	0/78/105
<i>US-NGB</i> ¹⁴²	SNO	2013-2023	529.6	0/108	0/0/70
<i>US-NGC</i> ¹⁴³	GRA	2017-2023	409.9	0/61	0/0/43
<i>US-NR1</i> ¹⁴⁴	ENF	2013-2022	1228.2	0/175	0/0/294
<i>US-NR3</i> ¹⁴⁵	GRA	2014-2023	0.0	847/0	0/0/0
<i>US-NR4</i> ¹⁴⁶	GRA	2014-2023	938.2	0/165	0/0/311
<i>US-ONA</i> ¹⁴⁷	GRA	2016-2022	0.0	0/0	962/0/0
<i>US-ORv</i> ¹⁴⁸	WET	2013-2016	243.4	0/50	0/0/22
<i>US-OWC</i> ¹⁴⁹	WET	2016-2023	0.0	0/0	171/0/0
<i>US-Oho</i> ¹⁵⁰	DBF	2013-2013	0.0	121/0	0/0/0
<i>US-PSH</i> ¹⁵¹	DBF	2016-2017	0.0	66/0	0/0/0
<i>US-PSL</i> ¹⁵²	DBF	2016-2017	0.0	0/0	0/62/0
<i>US-Pnp</i> ¹⁵³	WAT	2016-2022	188.6	0/0	0/17/33
<i>US-Prr</i> ¹⁵⁴	ENF	2013-2022	985.3	0/0	0/120/166
<i>US-RGA</i> ¹⁵⁵	CRO	2021-2023	0.0	340/0	0/0/0
<i>US-RGB</i> ¹⁵⁶	CRO	2021-2023	225.4	0/0	0/157/46
<i>US-RGF</i> ¹⁵⁷	CRO	2023-2023	59.8	0/0	0/0/18
<i>US-RGW</i> ¹⁵⁸	CRO	2022-2023	58.9	0/0	0/147/17
<i>US-RGo</i> ¹⁵⁹	CRO	2021-2023	0.0	0/0	386/0/0
<i>US-Rls</i> ¹⁶⁰	CSH	2014-2022	1598.9	0/300	0/0/348
<i>US-Rms</i> ¹⁶¹	CSH	2014-2022	1513.7	0/0	0/277/321
<i>US-Ro1</i> ¹⁶²	CRO	2014-2017	0.0	435/0	0/0/0
<i>US-Ro2</i> ¹⁶³	CRO	2015-2017	0.0	0/0	317/0/0
<i>US-Ro4</i> ¹⁶⁴	GRA	2015-2023	0.0	0/0	1657/0/0
<i>US-Ro5</i> ¹⁶⁵	CRO	2017-2023	0.0	1455/0	0/0/0
<i>US-Ro6</i> ¹⁶⁶	CRO	2017-2023	0.0	0/0	1445/0/0
<i>US-Rpf</i> ¹⁶⁷	DBF	2013-2022	1293.8	0/0	0/178/242
<i>US-Rwf</i> ¹⁶⁸	CSH	2014-2022	1593.7	0/296	0/0/345
<i>US-Rws</i> ¹⁶⁹	OSH	2014-2022	0.0	2209/0	0/0/0
<i>US-SP1</i> ¹⁷⁰	ENF	2013-2020	653.4	0/0	0/129/137

<i>US-SRC</i> ¹⁷¹	OSH	2013-2014	0.0	0/83	0/0/0
<i>US-SRG</i> ¹⁷²	GRA	2013-2023	0.0	3057/0	0/0/0
<i>US-SRM</i> ¹⁷³	WSA	2013-2023	1659.9	0/0	0/162/393
<i>US-SRS</i> ¹⁷⁴	WSA	2013-2018	1026.5	0/0	0/231/184
<i>US-SSH</i> ¹⁷⁵	DBF	2016-2021	302.0	0/0	0/120/119
<i>US-Seg</i> ¹⁷⁶	GRA	2013-2023	2102.4	0/0	0/276/446
<i>US-Ses</i> ¹⁷⁷	OSH	2013-2023	0.0	2638/0	0/0/0
<i>US-Slt</i> ¹⁷⁸	DBF	2013-2014	132.9	0/0	0/200/17
<i>US-Snd</i> ¹⁷⁹	GRA	2013-2015	119.8	0/0	0/149/0
<i>US-Sne</i> ¹⁸⁰	GRA	2016-2020	0.0	561/0	0/0/0
<i>US-Snf</i> ¹⁸¹	GRA	2018-2020	114.5	0/139	0/0/26
<i>US-Srr</i> ¹⁸²	WET	2014-2017	0.0	445/0	0/0/0
<i>US-StJ</i> ¹⁸³	WET	2015-2017	0.0	766/0	0/0/0
<i>US-Syv</i> ¹⁸⁴	MF	2013-2023	494.5	0/71	0/0/114
<i>US-Tw1</i> ¹⁸⁵	WET	2013-2022	0.0	874/0	0/0/0
<i>US-Tw2</i> ¹⁸⁶	CRO	2013-2013	13.3	0/0	0/0/0
<i>US-Tw3</i> ¹⁸⁷	CRO	2013-2018	484.4	0/0	0/161/77
<i>US-Tw4</i> ¹⁸⁸	WET	2013-2022	978.2	0/0	0/143/223
<i>US-Tw5</i> ¹⁸⁹	WET	2018-2020	53.6	0/0	0/87/14
<i>US-Twt</i> ¹⁹⁰	CRO	2013-2017	331.1	0/113	0/0/46
<i>US-UM3</i> ¹⁹¹	WAT	2013-2014	41.6	0/0	0/42/4
<i>US-UMB</i> ¹⁹²	DBF	2013-2014	39.5	0/0	0/88/22
<i>US-UTB</i> ¹⁹³	BSV	2021-2023	25.3	0/0	0/96/13
<i>US-Uaf</i> ¹⁹⁴	ENF	2013-2022	0.0	833/0	0/0/0
<i>US-Var</i> ¹⁹⁵	GRA	2013-2023	0.0	0/0	2612/0/0
<i>US-Vcm</i> ¹⁹⁶	ENF	2013-2023	1712.2	0/0	0/221/372
<i>US-Vcp</i> ¹⁹⁷	ENF	2013-2023	1165.7	0/0	0/159/284
<i>US-Vcs</i> ¹⁹⁸	ENF	2016-2023	0.0	1894/0	0/0/0
<i>US-WPT</i> ¹⁹⁹	WET	2013-2013	0.0	0/0	163/0/0
<i>US-Whs</i> ²⁰⁰	OSH	2013-2023	0.0	2610/0	0/0/0
<i>US-Wjs</i> ²⁰¹	SAV	2013-2023	2193.8	0/263	0/0/425
<i>US-Wkg</i> ²⁰²	GRA	2013-2023	1788.8	0/0	0/284/419
<i>US-Wrc</i> ²⁰³	ENF	2013-2016	415.7	0/0	0/243/81
<i>US-xAB</i> ²⁰⁴	ENF	2017-2022	182.1	0/118	0/0/42
<i>US-xAE</i> ²⁰⁵	GRA	2019-2022	224.4	0/138	0/0/71
<i>US-xBA</i> ²⁰⁶	WET	2017-2022	170.8	0/35	0/0/46
<i>US-xBL</i> ²⁰⁷	DBF	2017-2022	213.8	0/0	0/122/71
<i>US-xBN</i> ²⁰⁸	ENF	2017-2022	231.8	0/75	0/0/39
<i>US-xBR</i> ²⁰⁹	DBF	2017-2022	436.8	0/0	0/117/116
<i>US-xCL</i> ²¹⁰	GRA	2018-2022	233.4	0/128	0/0/42
<i>US-xCP</i> ²¹¹	GRA	2017-2022	0.0	0/0	456/0/0
<i>US-xDC</i> ²¹²	GRA	2017-2022	0.0	876/0	0/0/0
<i>US-xDJ</i> ²¹³	ENF	2017-2022	0.0	611/0	0/0/0
<i>US-xDL</i> ²¹⁴	MF	2017-2022	163.7	0/93	0/0/13
<i>US-xDS</i> ²¹⁵	CVM	2018-2022	289.7	0/0	0/77/41
<i>US-xGR</i> ²¹⁶	DBF	2017-2022	230.7	0/106	0/0/41
<i>US-xHA</i> ²¹⁷	DBF	2017-2022	0.0	458/0	0/0/0
<i>US-xHE</i> ²¹⁸	OSH	2017-2022	303.5	0/172	0/0/61
<i>US-xJE</i> ²¹⁹	ENF	2017-2022	307.7	0/0	0/129/67
<i>US-xJR</i> ²²⁰	OSH	2017-2022	0.0	0/0	490/0/0
<i>US-xKA</i> ²²¹	GRA	2017-2022	285.9	0/0	0/117/60
<i>US-xKZ</i> ²²²	GRA	2017-2022	368.2	0/114	0/0/69
<i>US-xLE</i> ²²³	DBF	2017-2022	56.2	0/79	0/0/2

<i>US-xMB</i> ²²⁴	OSH	2019-2022	188.5	0/119	0/0/33
<i>US-xML</i> ²²⁵	DBF	2019-2022	0.0	0/0	275/0/0
<i>US-xNG</i> ²²⁶	GRA	2017-2022	308.6	0/111	0/0/70
<i>US-xNQ</i> ²²⁷	OSH	2019-2022	0.0	0/0	332/0/0
<i>US-xNW</i> ²²⁸	ENF	2018-2022	0.0	0/0	276/0/0
<i>US-xRM</i> ²²⁹	ENF	2017-2022	417.0	0/0	0/139/100
<i>US-xRN</i> ²³⁰	DBF	2019-2022	0.0	0/0	304/0/0
<i>US-xSB</i> ²³¹	ENF	2019-2022	0.0	0/0	240/0/0
<i>US-xSC</i> ²³²	DBF	2020-2022	0.0	0/0	187/0/0
<i>US-xSE</i> ²³³	DBF	2017-2022	0.0	389/0	0/0/0
<i>US-xSJ</i> ²³⁴	SAV	2019-2022	175.1	0/0	0/97/35
<i>US-xSL</i> ²³⁵	CRO	2017-2022	191.3	0/128	0/0/32
<i>US-xSP</i> ²³⁶	ENF	2017-2022	0.0	0/0	383/0/0
<i>US-xSR</i> ²³⁷	OSH	2017-2022	236.8	0/0	0/128/67
<i>US-xST</i> ²³⁸	DBF	2017-2022	0.0	878/0	0/0/0
<i>US-xTA</i> ²³⁹	ENF	2017-2022	0.0	0/0	450/0/0
<i>US-xTL</i> ²⁴⁰	WET	2017-2022	141.9	0/0	0/77/61
<i>US-xTR</i> ²⁴¹	DBF	2017-2022	374.8	0/98	0/0/73
<i>US-xUK</i> ²⁴²	DBF	2017-2022	519.5	0/0	0/233/111
<i>US-xUN</i> ²⁴³	MF	2017-2022	398.4	0/110	0/0/76
<i>US-xWD</i> ²⁴⁴	GRA	2017-2022	288.4	0/127	0/0/79
<i>US-xWR</i> ²⁴⁵	ENF	2018-2022	233.2	0/0	0/89/53
<i>US-xYE</i> ²⁴⁶	ENF	2019-2022	222.1	0/0	0/126/25